Journal of
Synchrotron Radiation

ISSN 0909-0495

Received 19 January 2007
Accepted 10 March 2007

Element-selective X-ray detected magnetic resonance: a novel application of synchrotron radiation

J. Goulon,[a]* A. Rogalev,[a] F. Wilhelm,[a] Ch. Goulon-Ginet[a,b] and G. Goujon[a]

[a]European Synchrotron Radiation Facility, BP 220, F-38043, Grenoble, France, and [b]Faculté de Pharmacie, Université J. Fourier, F-38700 La Tronche, France. E-mail: goulon@esrf.fr

X-ray detected magnetic resonance (XDMR) is a new element-selective spectroscopy in which X-ray magnetic circular dichroism is used to probe the resonant precession of spin and orbital magnetization components when a strong microwave pump field is applied perpendicularly to the static bias field. Experimental configurations suitable for detecting the very weak XDMR signal are compared. XDMR signatures were measured in yttrium iron garnet and related thin films on exciting not only the iron *K*-edge but also the yttrium at diamagnetic sites. These measurements are shown to yield unique information regarding the wide-angle precession of induced magnetization components involving either orbital *p*-projected densities of states at the iron sites, or spin polarized *d*-projected densities of states at the yttrium sites. Extending XDMR measurements into the millimeter wave range would make it possible to study paramagnetic systems routinely and investigate optical modes as well as acoustic modes in ferrimagnetic/antiferromagnetic systems.

Keywords: X-ray absorption spectra; X-ray magnetic circular dichroism; ferromagnetic resonance; magneto-optical effects.

1. Introduction to X-ray magnetic circular dichroism

Since the pioneering work of Schütz and co-workers in the late 1980s (Schütz *et al.*, 1987), X-ray magnetic circular dichroism (XMCD) has become a well established tool for studying induced magnetism, especially in thin films and magnetic multilayers. A comprehensive review of this field was published recently with numerous references therein (Rogalev *et al.*, 2006). What stimulated interest in XMCD was the prospect of resolving the spin and orbital magnetization components at a selected absorbing element: this turned out to be possible within the limits of validity of the magneto-optical sum rules (Thole *et al.*, 1992; Carra, Thole *et al.*, 1993; Strange, 1994; Ebert *et al.*, 1999). In this paper we describe how, at third-generation synchrotron radiation sources, XMCD can be also used to probe the resonant precession of spin and orbital magnetization components in a strong microwave pump field (Bailey *et al.*, 2004; Goulon, Rogalev, Wilhelm *et al.*, 2005; Guan *et al.*, 2006; Goulon *et al.*, 2006*a*; Arena *et al.*, 2006). In this perspective, X-ray detected magnetic resonance (XDMR) can be seen as the extension into the X-ray regime of a spectroscopy widely known from its acronym ODMR (optically detected magnetic resonance) (*e.g.* Hanlon & Dillon, 1965; Borovik-Romanov *et al.*, 1980; Gnatzig *et al.*, 1987).

As illustrated in Fig. 1, one may envisage two different configurations for an XDMR experiment. In the longitudinal geometry, the wavevector $\mathbf{k}_X$ of the incident circularly polarized X-rays is parallel to the static magnetic bias field $\mathbf{B}_0$, whereas the microwave pump field $\mathbf{b}_p$ oscillates in a direction perpendicular to $\mathbf{B}_0$. As a first approximation, that will be shown later to be questionable, let us assume that the length of the equilibrium magnetization vector remains invariant in the precession: $M_s = |\mathbf{M}_{eq}|$. Then, one would expect a time-invariant change of the projection of the magnetization along the direction of $\mathbf{B}_0$, and the challenge of XDMR in the long-

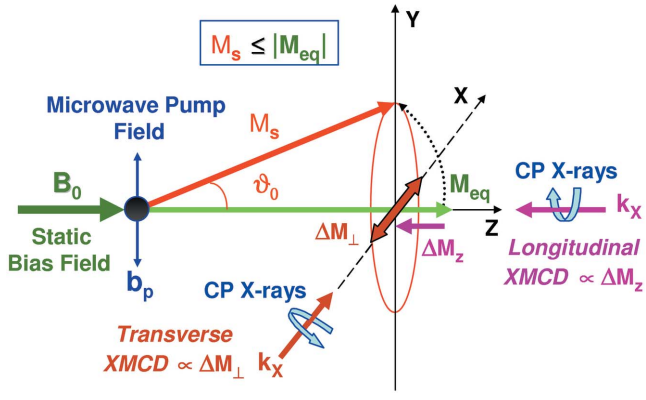

Figure 1
XDMR detection in longitudinal and transverse geometries. ΔM_z is time invariant only if $M_s = |\mathbf{M}_{eq}|$. Decreasing M_s would increase $|\Delta M_z|$.

itudinal geometry is precisely to probe ΔM_z using XMCD. Actually, ΔM_z is time invariant only for circular precession, while $|\Delta M_z|$ should increase if $M_s \leq |\mathbf{M}_{eq}|$. In the transverse geometry, the wavevector $\mathbf{k}_X$ of the incident circularly polarized X-rays would now be set perpendicular to both $\mathbf{B}_0$ and $\mathbf{b}_p$; what should then be measured is a stronger XMCD signal proportional to the transverse magnetization $\Delta M_\perp$ but which oscillates at the microwave frequency.

In our approach, the XMCD signal caused by precession is systematically recorded in the X-ray fluorescence excitation mode. An alternative detection scheme for XDMR has been explored since 2004 by Bailey *et al.* who combined time-resolved soft X-ray reflectometry with pulsed induction magnetometry. Subsequent work by the same group confirmed that XDMR spectra recorded in the time domain made it possible to access layer-resolved spectra in magnetic multilayers and to reveal weak ferromagnetic coupling (Arena *et al.*, 2006). The possibility of imaging ferromagnetic resonance eigenmodes excited at low frequency (250 MHz) was also demonstrated at ALS (Puzic *et al.*, 2005), again with soft X-rays. A tentative experiment to detect XDMR at the ESRF in the soft X-ray range should also be cited (Boero *et al.*, 2005), even though the XDMR signal did not appear to be totally inverted on switching the helicity of the X-ray photons from left to right.

In §2 we report on further instrumentation developments at the ESRF which make it now possible to record, on beamline ID12, high-quality XDMR spectra in the transverse configuration as well as in the longitudinal geometry. In §3 the performances of our instrumentation are illustrated with spectra recorded essentially at the *K*-edge of iron and *L*-edges of yttrium in yttrium iron garnet (YIG) and related thin films. Recall that, at the *K*-edges of transition metals, the XMCD signal is typically two orders of magnitude weaker than at the corresponding *L*-edges measured in the soft X-ray range. This makes XDMR much more demanding in terms of the instrumentation performances, but the advantage gained in return is that we may access the true magnetic properties of the bulk material since we are much less sensitive to surface effects than with soft X-rays. The information content of XDMR spectra is discussed in §4. In particular, we insist on the unique property of *K*-edge XDMR measurements which is to probe the precession dynamics of only orbital magnetization components while it is not straightforward to extract similar information at spin–orbit split *L*-edges. Finally, we give some prospective indications of the directions along which XDMR experiments could develop in the years to come at the ESRF.

2. ESRF XDMR spectrometer

2.1. Longitudinal or transverse detection

Given that the opening angle θ_0 of precession is very small in a conventional ferromagnetic resonance (FMR) experiment, one may prefer to detect XDMR in the transverse geometry because the signal is proportional to $\sin\theta_0$ whereas it is only a second-order effect proportional to $\tan^2\theta_0$ in the longitudinal geometry. What made, initially, the longitudinal geometry more attractive to us was the argument that no fast X-ray detector was needed since ΔM_z is essentially proportional to the microwave power which can be amplitude modulated at low frequency (F_m). Another key argument was given a long time ago by Bloembergen and co-workers (see Bloembergen & Wang, 1954), who pointed out that the longitudinal geometry was much less sensitive to magnon–magnon scattering processes in FMR so that one could benefit from a much higher saturation limit regarding the pumping power. Those considerations convinced us to give the highest priority to XDMR measurements in the longitudinal geometry.

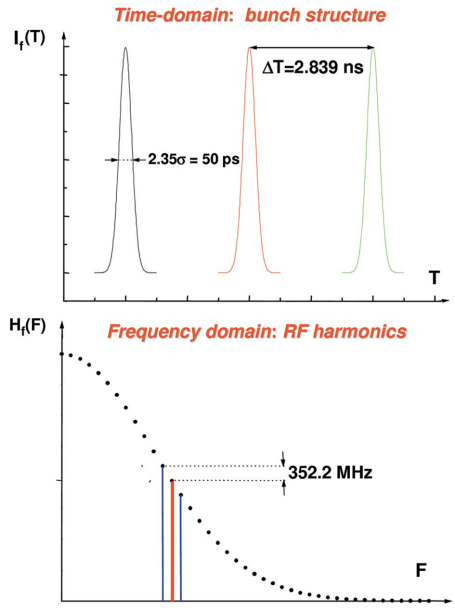

Figure 2
X-ray fluorescence intensity detected in the time and frequency domains.

Even though standard X-ray fluorescence detectors, especially those which have a large active area, are not suitable for detecting a small XMCD signal oscillating at microwave frequency, we want to show here that XDMR signals can still be measured in the transverse geometry using an heterodyne (beating) method. As illustrated in Fig. 2, let us recall that the time structure of the excited X-ray fluorescence signal $I_f(T)$ consists of a series of discrete bunches, with a periodicity ΔT = 2.839 ns directly related to the RF frequency (352.202 MHz) of the storage ring, and with a full width at half-maximum (FWHM) length of ~50 ps at the ESRF,

$$I_f(T) = I_{f_0} \sum_n \delta(T - n\Delta T)\, \frac{1}{\sigma(2\pi)^{1/2}}\, \exp\left(-T^2/2\sigma^2\right).$$

On Fourier transforming $I_f(T)$, one obtains in the frequency domain a Gaussian envelope of harmonics of the RF frequency (Gratton, 1992),

$$H_f(F) = \frac{I_{f_0}}{\Delta T} \sum_n \delta\left(F - \frac{n}{\Delta T}\right) \exp\left[-2(\pi\sigma F)^2\right].$$

One could easily check that the half width at half-maximum of the Gaussian envelope corresponds typically to the 25th harmonics of the RF frequency. At the ESRF, 25 × RF = 8.79 GHz is a typical frequency in the microwave X-band. It was therefore our idea to attempt to detect the beating signature of the transverse XMCD signal with the closest harmonics of the RF frequency. In other terms, it was proposed to adapt to our case the (super-)heterodyne detection of magnetic resonance that was quite common in the early 1960s, but with the tremendous advantage that synchrotron radiation directly provides us with a local microwave oscillator very near the desired XDMR frequency.

In this new approach of XDMR, the resonance frequency of the microwave cavity should obviously match as closely as possible the frequency of selected harmonics (*i.e.* n = 3, 8, 12, 16, 24 . . .). Special resonators were thus carefully optimized for these experiments which also require a very high frequency stability and a very low phase noise. In the present paper we shall report on a first experiment carried out in the transverse geometry using the 24th harmonics of the RF frequency. An unexpected difficulty arose because the RF frequency is one parameter (among others) that is used by the accelerator physicists to stabilize the electron orbit in the storage ring. In real practice, the RF frequency is being re-adjusted from time to time by small increments $\Delta_{RF} \simeq 1$ Hz with the undesirable consequence that our beating frequency will vary accordingly by $24 \times \Delta_{RF} \simeq 24$ Hz jumps. As shown in §3.4, such RF re-adjustments would spoil the sensitivity of the XDMR experiment in the transverse geometry. In collaboration with Agilent Technologies, a multichannel vector spectrum analyzer (VSA) operated as a digital lock-in has been designed to eliminate this difficulty. Another strategy which proved to be almost as efficient was to monitor permanently the RF frequency and to correct the microwave frequency in order to keep the beating frequency constant over long data acquisition times.

Let us emphasize that there is no fundamental reason why XDMR measurements in the longitudinal geometry could not be extended up to the sub-THz region, *e.g.* using high-power pulsed gyrotron sources that are now commercially available. The extension of the heterodyne detection of XDMR towards the millimeter wave range is more delicate to envisage because it would require synchrotron radiation sources with shorter bunch lengths in the time domain. At present, given the specifications of the ESRF storage ring, the sensitivity of the method will drop down to above 20 GHz. Nevertheless, this limit could potentially be extended up to very high frequencies if the bunch length (2.35σ) could be decreased to the sub-picosecond range, *e.g.* at a fourth-generation synchrotron radiation source.

2.2. Microwave bridge and cavities

The decision was made to build at the ESRF a spectrometer designed to routinely record XDMR spectra at high microwave pumping power over the whole microwave frequency range 1–18 GHz. Even though the first measurements were performed in the longitudinal geometry, it was anticipated that this spectrometer should ultimately be operated in the transverse geometry as well, but only at a few discrete microwave frequencies. This XDMR equipment is now permanently installed on beamline ID12 which was optimized to record high-quality XMCD spectra at the *K*-edges of all 3*d* transition metals as well as at the *L*-edges of the rare-earths and all 4*d*–5*d* transition elements (Goulon *et al.*, 1998). The X-ray sources are powerful helical undulators delivering high photon fluxes over the whole energy range 1.8–18 keV.

A schematic arrangement of the microwave bridge used in the X-band is shown in Fig. 3. The microwave source is a wide-band generator with a very low phase noise (Anritsu MG-3692A). One may select various types of amplification stages depending on the level of required microwave pumping power: (i) a low-noise solid-state amplifier (Miteq AMF-4B) can deliver up to 34 dBm (2.5 W) for standard experiments; (ii) a microwave power module (Litton MPM-1020) based on a micro-TWT device can deliver up to 50 dBm (100 W).

Whenever higher pumping power is required, the MPM-1020 module can be replaced by a more powerful TWT amplifier (TMD Technologies, PTC6357) operated in the pulsed mode and which can deliver up to 69 dBm (8 kW) peak power in the X-band with

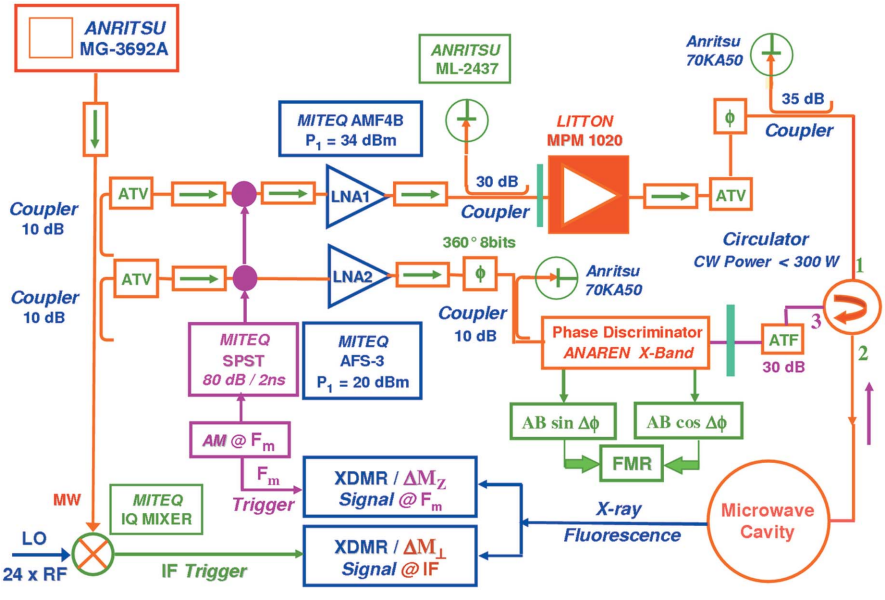

Figure 3
X-band microwave bridge used to detect XDMR spectra either in longitudinal or transverse detection modes.

a duty cycle of 5%. For the measurements on YIG thin films which are discussed in §3, there was no need for such high-power levels and the second amplification stage was simply by-passed. A circulator (Channel Microwave) compatible with the use of high microwave power is used to extract the microwave signal reflected back from the microwave cavity. This signal and an amplified component from the reference arm are fed together into a phase discriminator (Anaren 20758) in order to record conventional FMR spectra.

For XDMR experiments in longitudinal geometry, the microwave power is square-wave modulated using a fast switch (Miteq, SPST 124796) featuring over 80 dB isolation with a very short rise/fall time ($\leq$2 ns). The modulation signal is generated from the RF reference of the ESRF storage ring using a home-made digital frequency divider. For XDMR experiments in the transverse geometry, the 24th harmonics of the RF are produced on combining a low-noise frequency tripler (Wenzel Associates, LNOM-352-3) with an active $\times$8 frequency multiplier (Miteq, SYS8$\times$80108). The latter 24th harmonics of the RF are fed into the local oscillator (LO) input of a quadrature IF mixer (Miteq, IR0810B27P), whereas the microwave reference is fed into the other RF input. The I/Q output signals (phase balance: $\pm 2^{\circ}$) are used for triggering a multichannel VSA (Agilent Technologies, VSA 89600-SU) in the time-average mode.

All experiments are performed on inserting the sample into home-made TE_{102} rectangular X-band cavities. For XDMR experiments carried out in the longitudinal geometry, the resonance frequency of the empty cavity was typically $F_{cav} \simeq 9.450$ GHz with $Q_L \leq 4300$; for XDMR experiments in the transverse geometry, the resonance frequency of the empty cavity was $F_{cav} \simeq 8.4517$ GHz with Q_L still in excess of 4000.

In recent months the sensitivity and the performances of the XDMR spectrometer were quite significantly improved thanks to a new cavity design (Fig. 4) in which the X-ray fluorescence photons could be collected in the back-scattering geometry that proved to be ideal for standard XMCD measurements. In this new design the electrical continuity of the cavity walls was preserved using a polished Be window (diameter 31 mm, thickness 25 µm) which made it also possible to collect the X-ray fluorescence photons over a large solid angle using a photodiode located very close to the sample. The photodiodes designed for this experiment have a large active area (300 mm^2) and a 4 mm-diameter hole at their center to allow the incident X-ray beam to pass through the Si wafer and enter the microwave cavity (Goulon, Rogalev, Goujon *et al.*, 2005). This new design did not simply allow us to increase the detection efficiency but it also made it possible to set $\mathbf{B}_0$ almost perpendicular to the YIG film with the advantage that larger precession angles could potentially be reached in the longitudinal detection mode.

Other types of resonant structures are still being investigated at the ESRF such as loop-gap resonators (Froncisz & Hyde, 1982; Pfenninger *et al.*, 1988) or low-Q microstrip resonators (Charbois, 2003; Boero *et al.*, 2005). Since the minimization of the dead-time after pulse is not the key issue in XDMR, the benefits are not as clear as for pulsed EPR or

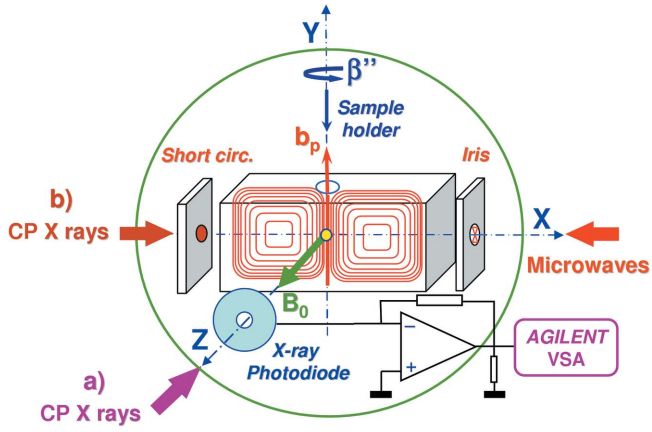

Figure 4
Experimental configuration for XDMR experiments using a TE_{102} rectangular cavity: (*a*) longitudinal detection; (*b*) transverse (heterodyne) detection.

FMR experiments. We are nevertheless thinking of using them but only for specialized XDMR applications in the microwave L- or S-bands ($F \leq 3$ GHz), whereas cavities offer better prospects for an extension of XDMR towards the millimeter wave range. Another advantage is in the possibility of freely rotating the sample inside the cavity without modifying the relative orientation of $\mathbf{B}_0$ and $\mathbf{b}_p$.

3. XDMR experiments

3.1. Samples: YIG thin films

YIG thin films provided us with a perfect testing ground for our first XDMR experiments and for evaluating the performances of our home-made instrumentation. Current thin-film technology makes it now possible to grow routinely on carefully selected substrates high-quality iron garnet thin films with a well controlled crystallinity and fairly narrow intrinsic FMR line-width: $\Delta B_{FWHM} \simeq 0.2$ G (Vittoria *et al.*, 1985). Moreover, on substituting partially the trivalent cations Y^{3+} with 'diamagnetic' rare-earth cations (*i.e.* La^{3+}, Lu^{3+}) or with Bi^{3+}, one may tailor the magnetic or magneto-optical properties of these films for specific technological applications requiring the equilibrium magnetization to be either perpendicular to the film surface or in the plane of the film. In magnetic thin films, the magneto-exchange spin wave spectra also become discrete, consisting of separate dispersion branches which are very sensitive to the film thickness. Regarding XMCD and XDMR experiments carried out in the X-ray fluorescence excitation mode, let us underline that the thin-film geometry makes the correction for fluorescence re-absorption particularly easy to handle while the thickness of the film can be selected to match nicely the X-ray penetration depth.

The iron garnet films used for the experiments reported in this paper were prepared at the Laboratoire de Magnétisme de Bretagne (Brest, France); all films were grown by liquid-phase epitaxy on gadolinium gallium garnet (GGG) crystals cut parallel either to the (111) or to the (100) planes. Given

that the film thickness was typically 5–10 µm, we are concerned below with bulk-like magnetic properties of these samples. For substituted films, the elemental composition was ascertained using microfluorescence analyses, while the crystal structure and orientation of each film were carefully checked using X-ray diffraction. Small samples (2 mm × 2 mm) were glued onto low-loss sapphire rods (diameter 4 mm) terminated by a flat surface making the desired tilt angle (β') with respect to the rod axis. With the primitive cavity design used for our very first XDMR experiment (Goulon, Rogalev, Wilhelm *et al.*, 2005), a polar rotation of the sample (*e.g.* $\beta' = 30^\circ$) was desirable to improve the detection efficiency. This is no longer necessary with the new cavity design even though we kept an old sample holder with a tilt angle of $\beta' = 6^\circ$ for all experiments reported below on the unsubstituted YIG film. For the measurements in the transverse geometry, a further azimuthal rotation (β'') of the sapphire rod about the *Y* axis (Fig. 4) was still required to maximize the detection efficiency; as justified in §3.2, the sample was then rotated at the magic angle ($\beta'' = 54.73^\circ$).

3.2. Static XMCD measurements

We have already pointed out elsewhere (Goulon *et al.*, 2006*a*) that XDMR measurements should be systematically combined with XMCD data. In longitudinal XDMR experiments, XMCD and XDMR data can be collected in strictly the same geometry. For XDMR experiments in the transverse mode, there is no static XMCD signal to be measured in the transverse plane and XMCD spectra have to be recorded with $\mathbf{k}_X$ parallel to $\mathbf{B}_0$. We have reproduced in Fig. 5 the XANES and XMCD spectra of a YIG film (film #520; thickness: e = 9.8 µm) grown on a GGG substrate cut parallel to the (111) plane and magnetized perpendicularly. For the measurements at the iron *K*-edge (Fig. 5*a*), the source was an Apple-II helical undulator (HU-38), but another undulator (EMPHU) combining electromagnet/permanent-magnet technologies (Rogalev *et al.*, 1999) was preferred for the experiments run at the yttrium *L*-edges (Figs. 5*b* and 5*c*). In both cases the two-crystal monochromator of ESRF beamline ID12 was equipped with a pair of Si (111) crystals cooled down to 140 K. The energy resolution was very close to the expected theoretical values: $\Delta E \simeq 1.15$ eV at the Fe *K*-edge; $\Delta E \simeq 0.32$ eV at the Y *L*-edges. Recall, however, that the repeatability of the Bragg scans converted into energy has to be better than 10 meV in order to warrant derivative-free XMCD spectra. All spectra were recorded in the fluorescence excitation mode and it should be stressed that the spectra reproduced in Fig. 5 are raw data, *i.e.* free of any corrections accounting for fluorescence re-absorption and polarization rates. As long as **M** is parallel to $\mathbf{k}_X$, we define the XMCD signal as the difference XMCD = $\{I_F^{(L)}/I_0^{(L)} - I_F^{(R)}/I_0^{(R)}\}$. Here, I_0 and I_F stand for the intensities of the incident beam and of the collected fluorescence photons for left (L) or right (R) circularly polarized incoming X-rays, the ratio I_F/I_0 defining the relevant reduced fluorescence intensity.

In YIG, the unit cell of the crystal consists of eight formula units: $\{Y\}_3[Fe]_2(Fe)_3O_{12}$. This formulation emphasizes the role of two non-equivalent sites for iron: the first one (16a sites) has octahedral coordination with oxygen anions, whereas the second one (24d sites) has tetrahedral coordination with those ligands (Gilleo, 1980). Below the Néel temperature (T_c = 550 K), the two Fe sublattices become antiferromagnetically ordered with an unbalanced magnetization ($\sim 5\mu_B$ per formula unit) in favour of the tetrahedral sites. It is not surprising therefore that a substantial XMCD signal can be observed at the iron *K*-edge. More puzzling was the observation of a rather strong XMCD signal at the yttrium *L*-edges. Let us mention here that intense XMCD signatures were detected as well at the *L*-edges of lanthanum and lutetium when the yttrium cations were partially substituted with the latter rare earths. The origin and the information content of the XMCD signatures will be extensively discussed in a separate paper (Goulon *et al.*, 2007) in which we conclude to the existence of induced spin components in the excited states of yttrium and related rare-earth atoms. Let us simply indicate here that the integrated spin moments (derived from the conventional magneto-optic sum rules) are, however, extre-

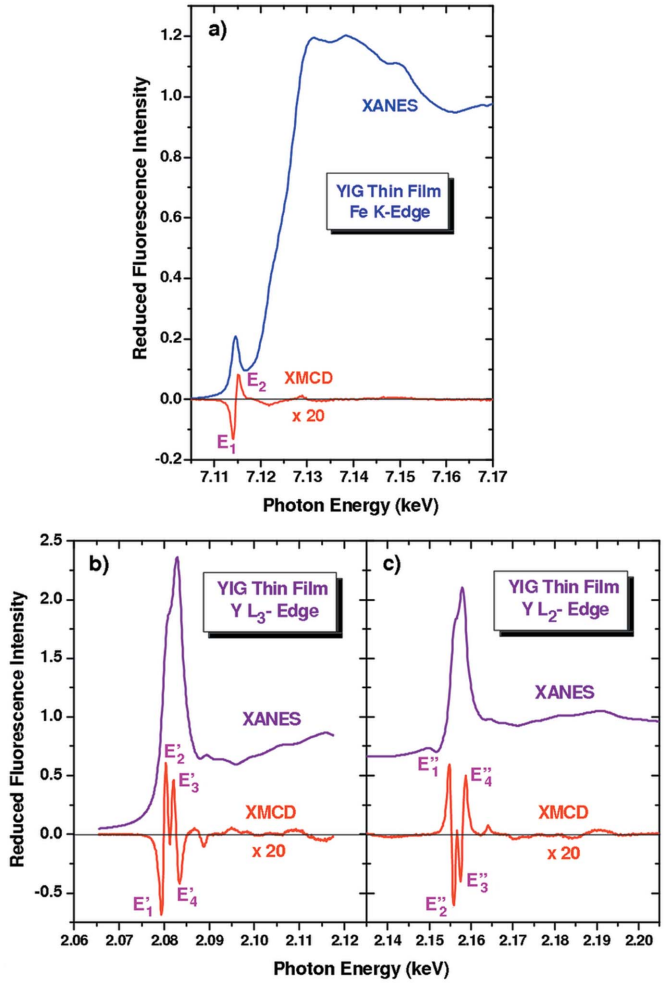

Figure 5
XANES and XMCD spectra of a perpendicularly magnetized YIG thin film: (*a*) Fe *K*-edge; (*b*) Y L_3-edge; (*c*) Y L_2-edge.

mely small. Having corrected an erroneous sign in the very preliminary analyses of our XMCD data (Goulon *et al.*, 2006*b*), we finally found that the 4*d* spin moment measured at the yttrium sites is always parallel to the applied bias field $\mathbf{B}_0$: the very weak spin moment induced at the diamagnetic yttrium sites (24c) should then align along the direction of the moment resulting from the unbalanced spin magnetization ($\sim 5\mu_B$) of the two iron sublattices. Super-exchange interactions mediated by the oxygen lattice should couple the spin moments induced on yttrium to the spin moments of the two iron sites.

For the XDMR experiments carried out at the Fe *K*-edge, the energy of the X-ray photons was tuned successively to E_1 = 7113.91 eV and E_2 = 7115.12 eV, *i.e.* to the two characteristic extrema of the XMCD signal in the pre-peak of the XANES spectrum. Similarly, the XDMR signatures were also measured at the successive extrema of the XMCD spectra recorded at the *L*-edges of yttrium (see Figs. 5*b* and 5*c*) or lanthanum. The so-called differential sum-rules introduced in §4 will precisely allow us to correlate the energies E_1, E_2 of Fig. 5(*a*) with the energies at which the *p*-projected densities of states (DOS) exhibit their largest orbital polarization at the iron sites. Similarly, the energies E_j', E_j'' in Figs. 5(*b*) and 5(*c*) will be correlated with the energies at which the *d*-projected DOS exhibit the maximum spin polarization at the yttrium sites.

3.3. Resonant pumping in the foldover regime

In any XDMR experiment, the first step invariably consists of recording conventional FMR spectra at modest microwave power. In the case of unsubstituted YIG thin films, these spectra exhibit a very rich pattern of sharp lines assigned to magnetostatic modes (Gurevich & Melkov, 1996; Charbois, 2003). Unfortunately, for samples that exhibit such intense and sharp FMR signals, measurements with high Q resonators often result in additional complications and spectral distortions. The main cause is that the reflected microwave intensity is given by a complex (homographic) function that is mixing the contributions of the real and imaginary parts of the complex magnetic susceptibility ($\chi'[B_0] + i\chi''[B_0]$) of the sample. This is illustrated in Fig. 6 in which we have reproduced the spectral dependence of the reflected microwave intensity when the bias field B_0 is scanned near resonance.

As shown in Fig. 6(*a*), we could recover a weakly distorted absorption spectrum on shifting the microwave frequency off resonance of the cavity by ΔF_{cav} = 3–7 MHz. This is known as a common trick to minimize radiation damping effects and avoid line-width broadening. Higher microwave fields and larger precession angles can still be obtained in tuning the microwave frequency closer to the resonance frequency of the cavity as measured when the sample is inserted but no external bias field is applied: this was done for transverse XDMR measurements ($\Delta F_{cav} \simeq 2$ MHz) although the FMR absorption spectrum looks strongly distorted (Fig. 6*b*).

For perpendicularly magnetized YIG thin films, we measured a very narrow line-width of the uniform mode:

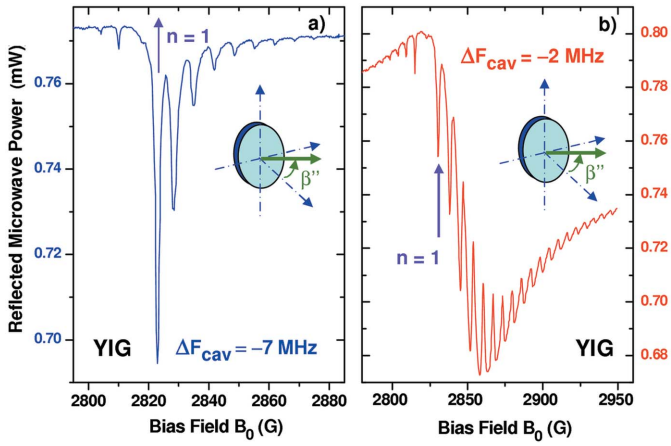

Figure 6
Instrumental distortions of FMR absorption spectra of a YIG thin film at modest microwave excitation power (6 mW): (*a*) far from the cavity resonance ΔF_{cav} = 7 MHz; (*b*) close to the cavity resonance ΔF_{cav} = 2 MHz. In both test experiments the normal to the YIG film was rotated away from the direction of the bias field B_0 by the azimuthal angle β'' = 54.73°.

$\Delta B_{FWHM}(\beta' = 0°) = 3^{1/2}\Delta B_{pp}$ = 1.13 G. As expected, the line-width increases with the polar tilt angle: ΔB_{FWHM} = 1.21 G for β' = 6°; 2.16 G for β' = 16° and finally 3.64 G for β' = 30°. With the azimuthal rotation of the sample at the magic angle (β'' = 54.73°), we could nevertheless keep a narrow line-width: $\Delta B_{FWHM} \simeq 2.1$ G. The line-width was also found to increase linearly as a function of the microwave frequency with the slope: 0.04 G GHz^{-1}. This figure can be converted into a dimensionless Gilbert damping factor of $\sim 6.0 \times 10^{-5}$ which confirms the high quality of the YIG film prepared in Brest.

For such a ferrimagnetic YIG film magnetized perpendicularly, the maximum precession angle $\theta_{0_{max}}$ at resonance is given by $\theta_{0_{max}} = 2b_{cp}/\Delta B_{FWHM}$, in which b_{cp} denotes the effective circularly polarized microwave pump field given by $b_{cp} \simeq (1/2)b_{lp}$ (see, for instance, Gnatzig *et al.*, 1987; Goulon *et al.*, 2006*a*). Obviously, YIG films are excellent test samples for XDMR owing to their very narrow line-widths. Nevertheless one has to increase the microwave power in order to scale b_p properly. In our experiments the incident microwave power was increased up to 28 dBm: this would correspond crudely to $b_p \simeq 0.35$ G. This implies that resonant pumping certainly occurred in the non-linear foldover regime in which resonance line-shapes are expected to be heavily distorted. The origin of foldover is discussed in standard FMR textbooks (*e.g.* Gurevich & Melkov, 1996) and its theory is rather clear in the case of a film magnetized perpendicularly (Bertotti *et al.*, 2001).

We have reproduced in Fig. 7 a numerical simulation which illustrates what might be the expected influence of foldover on the opening angle of precession (Gnatzig *et al.*, 1987; Goulon *et al.*, 2006*a*) under the conditions of our XDMR experiment. It is well documented that, in the foldover regime, $\theta_{0_{max}}$ can hardly be reached when the microwave power is amplitude modulated (Gnatzig *et al.*, 1987; Charbois, 2003). In the worst cases, the highest precession angle is found near the critical instability resonance field B_{C2} where the slope $d\theta_0/dB_0$ becomes infinite with $\theta_{0_{C2}} \ll \theta_{0_{max}}$ as marked in Fig. 7. For all

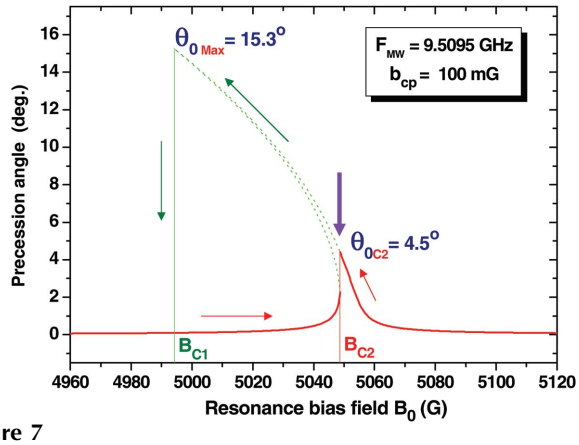

Figure 7
Simulated foldover line-shape for a perpendicularly magnetized YIG thin film.

experiments carried out in the longitudinal geometry with the magnetization almost perpendicular to the sample surface, the resonance field (B_0) was tentatively scanned down to the onset of the critical foldover jump, *i.e.* somewhere between B_{C1} and B_{C2}. The foldover jump measured in this way was found to slightly shift downwards on decreasing the microwave modulation frequency.

The spectral distortions associated with foldover are undesirable if we look for the ultimate sensitivity of the XDMR experiments. In the specific case of YIG films, it is well documented that the contribution of the uniaxial anisotropy field B_u (derived from a magnetic anisotropy free energy described by $\ell = 2$ spherical harmonics) largely exceeds the contribution of the cubic anisotropy B_{A1} (derived from a magnetic free energy described by $\ell = 4$ spherical harmonics). This implies that, at least in the case of YIG films, one could minimize the foldover effects on rotating the film near the magic angle (*e.g.* $\beta'' = 54.73°$) (J. Goulon, Ch. Brouder, A. Rogalev & F. Wilhelm, unpublished). The price to be paid, however, is that the precession is no longer circular but becomes elliptical. This was the choice we made for the transverse XDMR experiments discussed in §3.4, but it should be extended soon to future experiments to be carried out in the longitudinal geometry.

3.4. XDMR measurements in the longitudinal geometry

XDMR experiments in the longitudinal geometry were most easily carried out when the ESRF storage ring was operated in the 2 × 1/3 filling mode, *i.e.* with the X-ray beam square-modulated at a macrobunch repetition frequency: $F_{RX} = 2F_0 = 710.0846$ kHz in which F_0 = RF/992 is the revolution frequency of the electrons in the storage ring. As shown in Fig. 8, the modulation of the microwave power was carefully synchronized with the time-structure of the macrobunch: the microwave power is then square-modulated at a frequency $F_m = 2F_0/n$ kHz directly triggered from the RF master clock of the ESRF storage ring. In earlier experiments, we selected either $n = 20$ (Goulon, Rogalev, Wilhelm *et al.*, 2005) or $n = 25$ (Goulon *et al.*, 2006*b*) but we found it now preferable to use a

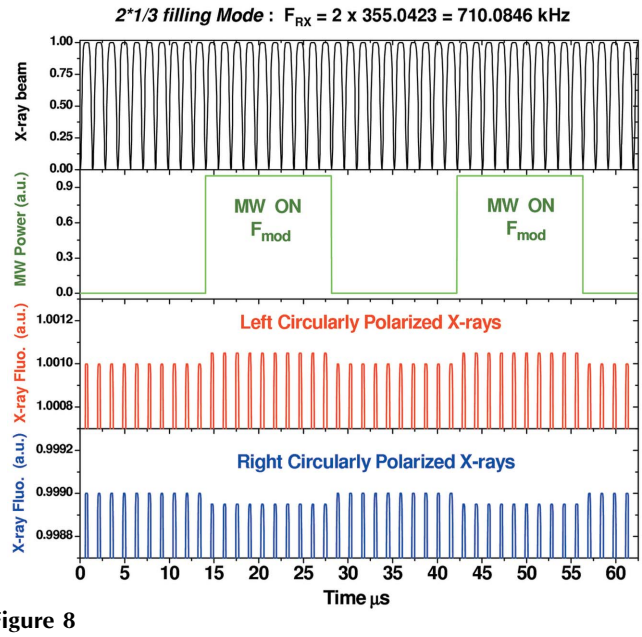

Figure 8
Synchronization of the microwave amplitude modulation with the time structure of the X-ray macrobunches in the 2 × 1/3 filling mode of the storage ring.

much lower modulation frequency ($n = 200$) in order to minimize the frequency span of the VSA.

The data acquisition was performed in the synchronous time-average mode of the VSA (Agilent Technologies, 89600-SU) driven by a triggering signal at F_m as discussed in §2.2. As expected, the XDMR signatures did appear as modulation sidebands at $F = F_{RX} \pm F_m$.

This is illustrated in Fig. 9(*a*) in which we have reproduced the typical frequency spectrum recorded while the YIG film was excited at $E_2 = 7115.1$ eV, *i.e.* near the Fe *K*-edge. We also display in Fig. 9(*b*) the cross-correlated spectral densities relative to the (positive/negative) frequency shifts. It immediately appears that the X-ray fluorescence signal at F_{RX} and the XDMR signal are peaking ∼115 dBV and 35 dBV above the noise floor, respectively; this gives a direct illustration of the very large dynamic range of our detection system. Note that the signal at F_{RX} is used mostly for intensity monitoring and data renormalization. Looking at $\mathrm{Re}[I_{XDMR}]$ and $\mathrm{Im}[I_{XDMR}]$, one could easily check that the XDMR signature is nicely inverted when the helicity of the incoming X-ray photons is switched from left to right (Goulon, Rogalev, Wilhelm *et al.*, 2005) or when the sign of the XMCD signal changes (Goulon *et al.*, 2006*b*).

With the same YIG sample, we also measured the XDMR signals at the yttrium $L_{2,3}$-edges: this experiment was particularly challenging because the flux and the circular polarization rate of the incident X-rays are much lower at 2.1 keV than at 7.1 keV, whereas the X-ray fluorescence yield at the Y *L*-edges is fairly poor. For the sake of brevity and space limitation, we have reproduced in Fig. 10 only the (+/−) cross-correlated spectral densities of the XDMR signals measured at the yttrium L_3- and L_2-edges, when the energy of the X-ray photons is tuned to the first extremum (E_1) of each relevant

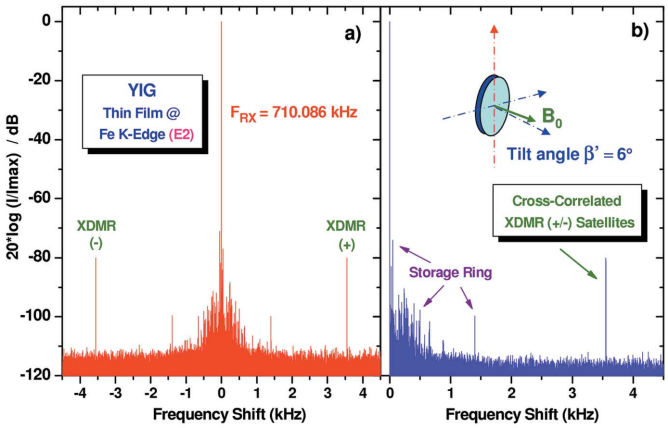

Figure 9
Longitudinal XDMR signal of the YIG film measured at the Fe K-edge for excitation energy E_2: (a) modulation sidebands detected at $F = F_{RX} \pm F_m$ with F_m = 3.55042 kHz; (b) cross-correlated spectral densities of the (+/−) modulation sidebands.

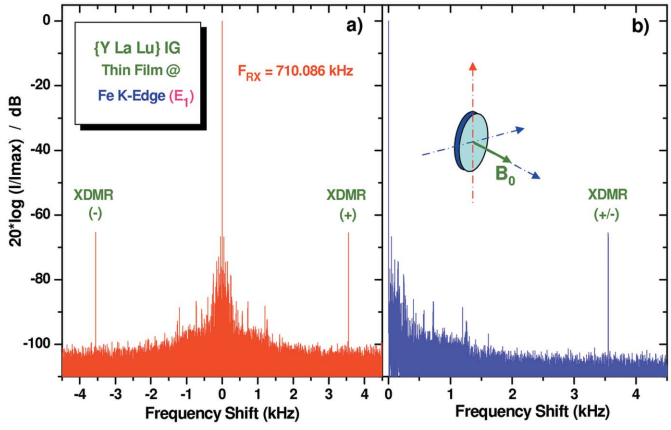

Figure 11
Longitudinal XDMR signal of the {Y, La, Lu}IG film measured at the Fe K-edge for excitation energy E_1: (a) modulation sidebands detected at $F = F_{RX} \pm F_m$ with F_m = 3.55042 kHz; (b) cross-correlated spectral densities of the ($\pm$) modulation sidebands.

XMCD spectrum. The geometry of the experiment, the incident microwave power and the resonant field B_0 were all kept strictly identical as for the previous measurements carried out at the Fe K-edge.

It clearly appears from Figs. 10(a) and 10(b) that the expected XDMR signatures are still peaking ∼18 dBV above the noise floor which was now kept fairly low (−126 dBV) whereas there is, indeed, a marked reduction of the amplitude of the peak at F_{RX} = 710.086 kHz monitoring the fluorescence intensity.

Further XDMR experiments concerned other garnet films in which the yttrium was partially substituted with lanthanum and lutetium. We shall report briefly here on additional results obtained with such a {Y, La, Lu}IG film of typical composition $Y_{1.3}La_{0.47}Lu_{1.3}Fe_{4.84}O_{12}$. Those XDMR experiments were carried out again in the longitudinal geometry but with $\beta' = \beta'' \simeq 0°$ whereas the microwave frequency was tuned somewhat closer to the resonance frequency of the cavity (ΔF_{cav} = 4 MHz).

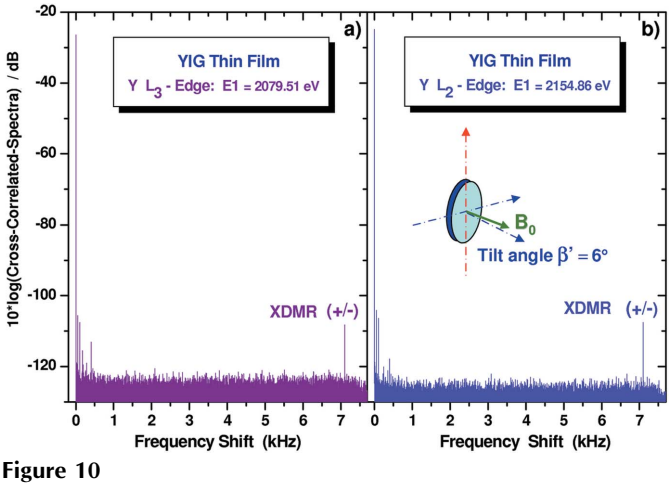

Figure 10
Cross-correlated (+/−) XDMR intensities measured in the longitudinal geometry at the Y $L_{2,3}$-edges for the excitation energy E_1: (a) Y L_3-edge XDMR signature; (b) Y L_2-edge XDMR signature.

On comparing Figs. 9 and 11, it immediately appears that there is a spectacular increase in the relative intensity of the XDMR signal (+14 dB). This gain in intensity can be explained by the stronger effective pump field experienced by the sample on approaching the resonance of the cavity. To a lower extent, the absence of any tilt angle should have also contributed to the observed enhancement. With an XDMR signal peaking ∼40 dB above the noise floor, we had enough dynamic reserve to scan the whole XDMR line in the foldover regime.

This is illustrated in Figs. 12(a) and 12(b), which reproduce the FMR and XDMR spectra that were both recorded simultaneously. The foldover distortion of the microwave absorption spectrum is fairly broad because the modulation frequency F_m = 3.55042 kHz was rather low. Note that the XDMR line-shape (Fig. 12b) exhibits a sharp increase very near the foldover jump while the FMR absorption spectrum (Fig. 12a) seems to saturate. The observed XDMR line-shape clearly indicates that what is measured in our experiment cannot be analyzed as a basic precession of the equilibrium magnetization: near saturation of the main resonance, it looks like the effective length (M_s) of the precessing magnetization vector would decrease and thus $|\Delta M_z|$ would increase. It has long been known that parametric amplification of spin waves takes place at high microwave power (Suhl, 1957, 1959). Typically, one expects four-magnon scattering processes to develop above a so-called second-order Suhl's instability threshold: these processes should limit the opening angle of precession and are well known to cause a saturation of the microwave susceptibility $\chi''[B_0]$, as observed experimentally. Let us mention, however, that the spectacular increase in $|\Delta M_z|$ which we observe in Fig. 12(b) could have the same origin as the anomalous increase in $|\Delta M_z|$ observed very recently by de Loubens and his colleagues (de Loubens *et al.*, 2005) again at the saturation of the main resonance with another YIG/GGG thin film, also grown in Brest. It was reported by these authors that not only $|\Delta M_z|$ but even the ratio $|\Delta M_z|/b_p^2$ would increase with power. They explained

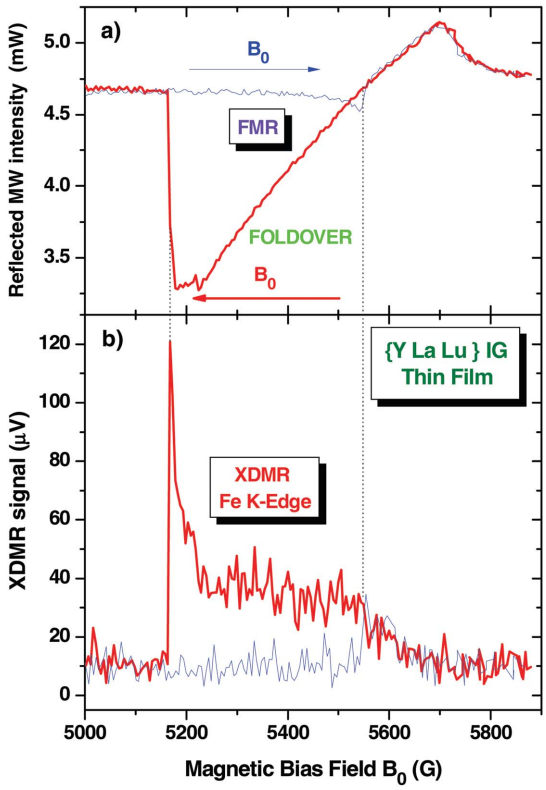

Figure 12
FMR and XDMR foldover line-shapes recorded with the {Y, La, Lu}IG film on scanning the bias field in both directions: (*a*) typical foldover line-shape of the microwave absorption spectrum; (*b*) XDMR line-shape measured under the same conditions on exciting the Fe *K*-edge at energy E_1.

this effect as being the consequence of a very weak damping of the longitudinal spin waves parametrically excited above the Suhl's instability threshold. Further discussion of the XDMR spectrum shown in Fig. 12(*b*) will take place in §4.1.3.

3.5. XDMR in transverse geometry

In this section we briefly report on the first XDMR experiment performed at the ESRF in the transverse geometry. This experiment was run while the ESRF machine was operated in the usual continuous filling mode, *i.e.* without any macrobunch time structure of the electron beam. Let us also mention here that, for that particular experiment, we tested a new type of sectorized photodiode, designed in collaboration with Canberra–Eurisys with the aim of benefiting a faster response and a reduced electronic noise level, but at the expense of a more complex multichannel readout electronics. Since each sector of the photodiode has its own readout electronics, we calculate systematically here the interchannel cross-correlated spectral densities minimizing the electronic noise. The data acquisition was again performed in the time-average mode of the multichannel VSA, using as triggering signal the IF outputs that were generated in phase quadrature, *e.g.* *I*/*Q*, in mixing externally the microwave signal with the 24th harmonics of the RF frequency as discussed in §2.2.

We have reproduced in Fig. 13(*a*) the transverse XDMR signal measured on exciting the YIG film at $E_2 = 7115.1$ eV, *i.e.* near the Fe *K*-edge. We checked very carefully that this signal was free of any artefact, *e.g.* it disappears completely if the X-ray beam shutter is closed or when the microwave power is turned off *etc.* Although the data acquisition time was shorter than in longitudinal XDMR experiments, the transverse XDMR signal is peaking here ∼45 dBV above the noise floor. Unfortunately, this detection scheme did not allow us (yet) to monitor simultaneously the fluorescence intensity as in the case of the longitudinal XDMR experiments discussed in the previous section.

Let us insist that the spectrum displayed in Fig. 13(*a*) could not be obtained without maintaining artificially the beating frequency constant. In other words, the RF frequency was permanently monitored during the data acquisition and the microwave frequency was re-adjusted in real time whenever a change in the RF

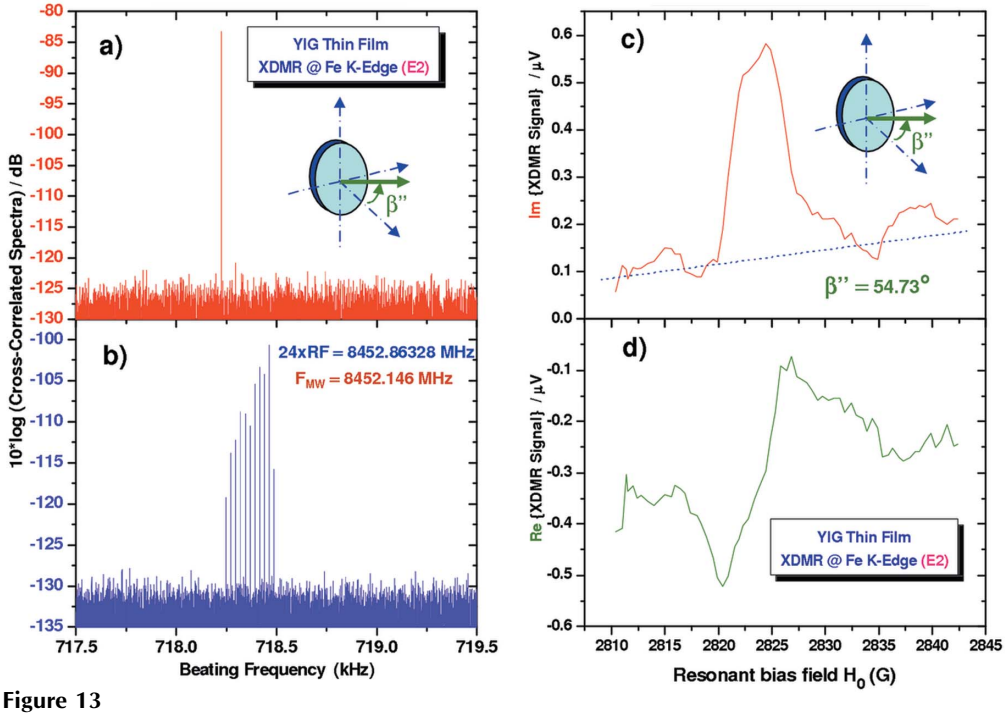

Figure 13
Fe *K*-edge XDMR spectra recorded in the transverse geometry using a YIG film rotated at the magic angle and excited at X-ray photon energy E_2: (*a*) XDMR signal recorded in the heterodyne detection mode while maintaining the beating frequency constant; (*b*) drifting XDMR signatures owing to RF instabilities. Field-scanned XDMR spectra: (*c*) $\mathrm{Im}[I_{\mathrm{XDMR}}]$; (*d*) $\mathrm{Re}[I_{\mathrm{XDMR}}]$.

frequency was detected. Fig. 13(*b*) was included to show what happens if the microwave frequency is kept unchanged: one clearly observes a series of discrete XDMR signatures, each of which is separated from the previous one by 24 Hz, as expected for deterministic variations of the RF frequency. Note that the phase and amplitude information become irremediably distorted or even lost in the time-average data acquisition mode when the beating frequency is unlocked. It is therefore very important to solve this problem properly if one wishes to be able to detect small phase differences between the various magnetization components precessing at different absorbing sites.

Taking full advantage of the higher sensitivity of the transverse XDMR signal, we attempted to record field-swept XDMR spectra at the Fe *K*-edge. This required us to speed up the data acquisition time by a factor of 20 compared with the measurements displayed in Fig. 13(*a*). The imaginary part $\mathrm{Im}[I_{\mathrm{XDMR}}]$ and the real part $\mathrm{Re}[I_{\mathrm{XDMR}}]$ of the Fe *K*-edge XDMR signal are plotted as a function of the bias field in Figs. 13(*c*) and 13(*d*), respectively. These measurements concerned only the part of the FMR spectrum assigned to the resonance of the uniform mode. We found that, under the present experimental conditions, the line-widths of the XDMR and FMR spectra were quite comparable. At this stage, it should be kept in mind that we reduced quite significantly the foldover line-shape distortions on rotating the sample at the magic angle but we could not eliminate the weaker effects due to magnetocrystalline anisotropy which should still affect the measured XDMR spectrum.

4. Discussion

4.1. Precession dynamics

4.1.1. Opening angle of precession. For a ferromagnetic thin film with true uniaxial anisotropy and near-normal magnetization, the opening angle of precession is a constant of the motion, even in the foldover regime (Bertotti *et al.*, 2001). This consideration led us to propose (Goulon, Rogalev, Wilhelm *et al.*, 2005; Goulon *et al.*, 2006*a*) to determine the opening angle θ_0 on combining together normalized XDMR cross sections with static XMCD cross sections measured under identical conditions. For an XDMR experiment performed in the longitudinal detection geometry ($\mathbf{k}_{\mathrm{X}} = \mathbf{k}_{\parallel}$) on a film magnetized perpendicularly to the surface of the film, one easily obtains

$$\left[\Delta\sigma_{\mathrm{XDMR}}(k_{\parallel})\right]/\left[\Delta\sigma_{\mathrm{XMCD}}(k_{\parallel})\right] \simeq -1/2\tan^2\theta_0. \qquad (1)$$

Similarly, for an XDMR experiment performed in the transverse geometry ($\mathbf{k}_{\mathrm{X}} = \mathbf{k}_{\perp}$) with the same film (Goulon *et al.*, 2006*a*),

$$\left[\Delta\sigma_{\mathrm{XDMR}}(k_{\perp})\right]/\left[\Delta\sigma_{\mathrm{XMCD}}(k_{\parallel})\right] \simeq \tan\theta_0\sin(\omega t+\varphi_0). \qquad (2)$$

Here, the various $\Delta\sigma_j$ refer to differential X-ray absorption cross sections. What stimulated us to develop the present XDMR instrumentation was the consideration that, not only the opening angle of precession (θ_0), but also the phase (φ_0) could be element-selective probes of the micromagnetic dynamical properties of the system under investigation (Goulon *et al.*, 2006*a*).

Let us stress, however, that both (1) and (2) rely on the Landau–Lifshitz–Gilbert equation of motion and assume that the norm of the local magnetization vector (M_{s}) is invariant in the forced precession. This should be true as long as the microwave pump field does not exceed some instability limit to be detailed in §4.1.3. Apparently, this was the case for the longitudinal XDMR measurements carried out on the YIG film rather far from the cavity resonance, *i.e.* with $\Delta F_{\mathrm{cav}} \simeq 7$ MHz. At the Fe *K*-edge, the apparent angle of precession measured at the X-ray photon energy E_1 increased from 5.5° to 6.3° when the modulation frequency was decreased from 35.5 kHz to 3.55 kHz. This could be consistent with a small shift of the foldover jump field. Under strictly the same experimental conditions (*i.e.* identical geometry, same pumping power, $\Delta F_{\mathrm{cav}} \simeq 7$ MHz, $F_{\mathrm{m}} = 3.55$ kHz), we found, however, that the precession angles measured at excitation energies E_1 and E_2 of Fig. 5(*a*) were significantly different: 6.3° at excitation energy E_1 and 8.1° at excitation energy E_2. This difference is well above our error bars (∼0.2°). Clearly a full scan of the XDMR spectrum recorded as a function of the excitation energy would help us to refine this remarkable result. This could point to the fundamental difference that may exist between XDMR and FMR: whereas standard FMR is concerned with the dynamical properties in the magnetic ground state, XDMR is probing dynamical phenomena in excited states in which the relevant magnetization component may be coupled in a fairly different way to the lattice.

It would be tempting to relate the precession angles measured at a given absorbing atom (*e.g.* Fe) to a damping parameter such as the dimensionless Landau–Lifschitz–Gilbert (LLG) constant α_{Fe}. Unfortunately, for XDMR experiments performed in the non-linear foldover regime, there is no simple analytical formulation relating $\theta_{0_{\mathrm{C2}}}$ to such a LLG damping constant. Numerical simulations would require a careful calibration of the effective pump field b_{cp} at the sample location: more work is in progress in order to assess the validity of a reliable calibration method. At this stage we admit that comparisons between experiments carried out with different samples are still difficult if not impossible because the samples may not experience identical effective microwave pump fields: this was clearly not the case for the XDMR measurement on the {Y, La, Lu}IG film.

4.1.2. Longitudinal and transverse relaxation times. One may alternatively look for a steady-state solution of the phenomenological Bloch equations. Following the notations of Bloembergen & Wang (1954), one would obtain

$$\frac{M_z}{M_{\mathrm{eq}}} = \frac{4\omega^2 + T_2^2\Omega^{(-)}}{4\omega^2 + T_2^2\Omega^{(-)} + \frac{1}{2}\gamma^2 b_{\mathrm{cp}}^2 T_1 T_2 \Omega^{(+)}} \qquad (3)$$

in which $\Omega^{(\pm)} = \omega_0^2 \pm \omega^2 + T_2^{-2}$ and $\omega_0 = \gamma B_0$ is the resonance frequency. At resonance,

$$\frac{\sigma_{\rm XDMR}}{\sigma_{\rm XMCD}} = \frac{\Delta M_z}{M_{\rm eq}} = \frac{1}{1+\frac{1}{4}(\gamma b_{\rm cp})^2 T_1 T_2} - 1. \qquad (4)$$

This equation would allow us to expect that, very near saturation, the magnetization could be inverted at resonance with $\sigma_{\rm XDMR} \rightarrow -\sigma_{\rm XMCD}$. Actually, this property is commonly used in NMR or EPR, *e.g.* for spin–echo measurements of T_1 in pulsed mode. However, it has long been recognized that this saturation limit can hardly be reached in FMR, even at very high microwave power, because parametric amplification of spin waves would result in a premature saturation of the precession angle (Suhl, 1959). Far from saturation, one would obtain

$$\frac{\sigma_{\rm XDMR}}{\sigma_{\rm XMCD}} \simeq -\frac{1}{4}(\gamma b_{\rm cp})^2 T_1 T_2. \qquad (5)$$

Equation (5) was exploited experimentally in FMR by Fletcher *et al.* (1960) but well below the foldover threshold, *i.e.* under conditions that are not suitable for XDMR measurements. Unfortunately, $b_{\rm cp}$ has not been determined as yet accurately enough in our XDMR experiments to let us access the T_1T_2 product. On the other hand, let us recall that any attempt to extract T_2 directly from the XDMR line-width in the transverse geometry ($T_2 = 2/\gamma\Delta B_{\rm FWHM}$) might be also seriously blurred by residual foldover distortion at the magic angle.

Even though the Bloch–Bloembergen model does not strictly conserve the length of the magnetization vector ($M_{\rm s} \neq |\mathbf{M}_{\rm eq}|$), nor does it satisfy the fluctuation–dissipation theorem (Goulon *et al.*, 2006*a*), the corresponding formulation turned out to be very convenient in practice because it puts a special emphasis on key differences that exist between the longitudinal (T_1) and transverse (T_2) relaxation times: whereas T_1 describes how fast the magnetic energy is exchanged with the lattice as a consequence of magneto-elastic and spin–orbit coupling, T_2 is much more sensitive to any loss of coherence owing to the coupling of the uniform precession mode ($k = 0$) with degenerated magneto-exchange modes or spin waves ($k \neq 0$). In the Landau–Lifschitz–Gilbert limit, one should simply have $(T_2)^{-1} = (2T_1)^{-1}$, but real measurements show that the corresponding relaxation rates would rather follow a relationship of the type

$$\frac{1}{T_2} = \frac{1}{2T_1} + \frac{1}{T_{\rm D}}, \qquad (6)$$

in which $T_{\rm D}$ would encompass all processes decreasing the coherence of the precessing magnetization. In the corpuscular language, magnetic oscillations and waves are associated with quasiparticles (magnons) with energy $\varepsilon = \hbar\omega$ and quasi-momentum $\mathbf{p} = \hbar\mathbf{k}$. Indeed, magnon scattering does not alter the whole magnetic free energy; only processes involving direct or indirect coupling to the lattice phonons are energy dissipative. The various relaxation channels that are expected to contribute to XDMR relaxation are summarized in Fig. 14.

In YIG films as well as for other types of films, sample non-uniformities such as crystal defects, impurities, surface pits *etc.* have long been shown to favour two-magnon scattering

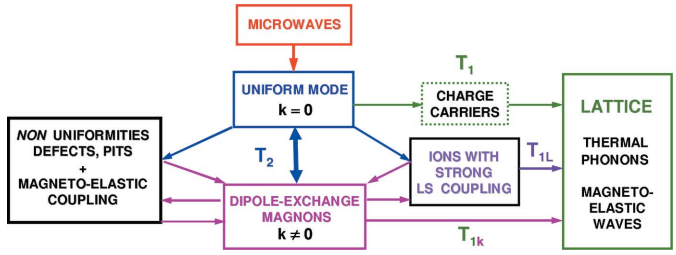

Figure 14
Block diagram of the various relaxation channels expected to contribute to XDMR (adapted from Gurevich & Melkov, 1996).

processes that increase the FMR line-width, especially at low resonance frequencies (Lenz *et al.*, 2006; Charbois, 2003; Gurevich & Melkov, 1996; Sparks, 1964). Three-magnon scattering processes (either in momentum splitting or confluence modes) do not conserve the total number of magnons nor they do conserve M_z: since the exchange Hamiltonian commutes with the operator associated with M_z, exchange thus cannot be involved in these processes. Three-magnon scattering processes are thus given to be rather weak but can nevertheless play a major role in specific geometries (*e.g.* parallel pumping of spin waves). In four-magnon scattering processes, two (uniform) magnons are annihilated but two magnons are created so that the total number of magnons remains unchanged. This has two consequences: (i) M_z will be conserved; (ii) the strong exchange interaction can be involved. We shall see in the next section that such processes play a central role in the theory of the saturation of FMR resonance.

Magneto-elastic interactions are the main cause of direct spin–lattice relaxation. In magnetically ordered systems, three-particle Cherenkov scattering processes involving two magnons plus one phonon are compatible with exchange interaction and form the most general basis of the analysis of direct spin–lattice relaxation mechanisms. In particular, the direct Cherenkov process (splitting of a magnon into another magnon plus one phonon) underlies the parametric excitation of magnetic and elastic waves under magnetic pumping (Gurevich & Melkov, 1996). In the case of ferrimagnetic insulators like YIG thin films, the Kasuya–LeCraw process (Kasuya & LeCraw, 1961) proved itself to be the most efficient mechanism to explain relaxation of magnetostatic magnons with very small k: it describes the confluence of a small-k magnon with a phonon from the upper (optical) branch to produce a magnon with large k that can now relax much more efficiently by a Cherenkov process. In the first step, the energy transfer does not occur from the spin system towards the lattice, but in the opposite direction with the benefit that a low-k magnon can be destroyed (Gurevich & Melkov, 1996). The Kasuya–LeCraw mechanism is most frequently given as the dominant contribution to T_1 and to the line-width in high-quality YIG thin films (see, for instance, Charbois, 2003).

In Fig. 14, we also emphasize the role of indirect spin–lattice relaxation processes mediated by ions featuring a large spin–orbit coupling and which may be responsible for giant anisotropy anomalies in FMR. YIG single crystals in which yttrium

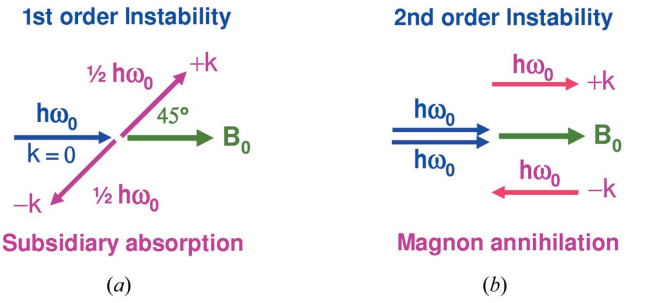

Figure 15
Schematic representation of Suhl's instability processes resulting in parametric amplification of spin waves. First-order (*a*) or second-order (*b*) instability thresholds were predicted from three-magnon or four-magnon scattering processes, respectively.

atoms are partly replaced by rare-earth cations with partially filled 4*f* shells are typical examples which were extensively studied 40 years ago (Gurevich & Melkov, 1996, and references therein). It has long been known that the FMR line-width is increasing rapidly in YIG films doped with transition-metal cations such as Fe^{2+}, Co^{2+}, Rh^{4+}, Ir^{4+} *etc.* in which spin–orbit coupling is important. In this respect, the slow longitudinal relaxation mechanism reviewed in detail by Van Vleck and others (Van Vleck, 1964; Hartmann-Boutron, 1964; Gurevich & Melkov, 1996, and references therein) should be of direct relevance to XDMR.

4.1.3. Premature saturation of precession. Given that the XDMR signals can only be measured at high microwave pumping power, one has to worry about non-linear effects resulting in the parametric amplification of spin waves as described by Suhl in his now classical papers (Suhl, 1957, 1959). As sketched in Fig. 15, he introduced two distinct instability thresholds associated either with a three-magnon or a four-magnon scattering process. While the first mechanism made it possible to understand the origin of a subsidiary absorption of microwaves off resonance, we are concerned in this paper with the non-linear second-order Suhl's instability connected with the saturation of the main resonance: two quanta of uniform precession ($k = 0$) split into two spin waves with equal but opposite momenta such that $2\omega_k = 2\omega_0$.

According to Suhl's prediction, a crude estimation of the critical pump field b_{c2} for saturation could be obtained from

$$b_{c2} \simeq \Delta B_{(0)}\left[\Delta B_{(k)}/\mu_0 M_s\right]^{1/2}, \qquad (7)$$

in which $\Delta B_{(0)}$ would refer to the intrinsic FMR line-width of the uniform mode ($k = 0$), while $\Delta B_{(k)}$ would denote the (poorly known) line-width of the amplified spin waves with momentum k. In order to tentatively explain the sharp increase of the XDMR signal in Fig. 12(*b*), we suggested that in our experiment the microwave pump field would most probably exceed b_{c2}. One should keep in mind, however, that the four-magnon scattering process will cause the annihilation of two uniform magnons, but will leave the total number of magnons unchanged. This has two major consequences: (i) we would expect the transverse XDMR signal, which probes only the uniform magnons, to exhibit a saturation effect just as in FMR; (ii) $|\Delta M_z|$ measured in the longitudinal XDMR geometry should be left unchanged because M_z is known to probe the total number of magnons (see Gurevich & Melkov, 1996). This is basically what was observed in the early 1950s by Bloembergen and co-workers (Damon, 1953; Bloembergen & Wang, 1954). Thus, it should be underlined that a two-magnon annihilation process alone cannot explain the sharp increase of the XDMR signal observed in Fig. 12(*b*): something else has to happen that is not yet taken into account.

The interpretation which we proposed in §3.4 was that there could be a reduction in the effective length of the magnetization vector, owing, for instance, to the parametric excitation of coupled magnetostatic/magnetoelastic waves (Gurevich & Melkov, 1996). In other terms, the opening angle of precession that would be calculated from the experiment shown in Fig. 11 should not be the true precession angle but only some apparent precession angle (Goulon *et al.*, 2007). Recall that de Loubens and co-workers (de Loubens *et al.*, 2005) observed a similar effect and proposed another interpretation scheme relying on the idea that the non-linear parametric amplification process would, in one way or another, favour among the spin waves those which have slow longitudinal relaxation rates compared with $1/T_1$. As a consequence, the average value of T_1 would increase and, according to equation (5), $|\Delta M_z|$ would also increase. Thus, in their approach, we would be left with this rather paradoxical situation where the XDMR line-width would be considerably broadened owing to the foldover effect, while the LLG damping parameter would decrease. Note that a similar behaviour might have been observed in permalloy as well (Yong An *et al.*, 2004). It remains to be clarified which mechanism could explain why the amplified spin waves should exhibit such a long T_1.

While Suhl's original theory considered exchange spin waves of short wavelengths, we wish to draw attention to some specificity of our experiment in which magnetostatic waves driven by dipolar interactions seem to play the key role. Using classical formulae for the dispersion laws of spin waves and magnetostatic waves (Gurevich & Melkov, 1996), we were able to simulate numerically the magnon spectra, either at very low microwave pumping power (Fig. 16*a*), or under the conditions of foldover as previously illustrated in Fig. 7. In a thin film magnetized perpendicularly, Fig. 16(*a*) shows that, at low pumping power, the uniform precession mode at resonance frequency F_0 falls at the bottom of the magnon band, *i.e.* where normal modes are not degenerated. Note that in Figs. 16(*a*) and 16(*b*), $1/2F_0$ is well below the magnon band anyway so that the three-magnon process associated with the first-order instability process cannot play any significant role at resonance, at least for the YIG thin films. On the other hand, it clearly appears that, under the conditions of foldover, the magnon band is slightly shifted down in Fig. 16(*b*): one immediately realises that long-wavelength longitudinal magnetostatic waves (*i.e.* with $\theta_k = 0, \pi$) can now be excited as a consequence of the foldover effect. This had already been anticipated a long time ago by Berteaud & Pascard (1966) to interpret their experiments on permalloy near saturation. In the regime described in Fig. 16(*b*), magnetic dipole–dipole

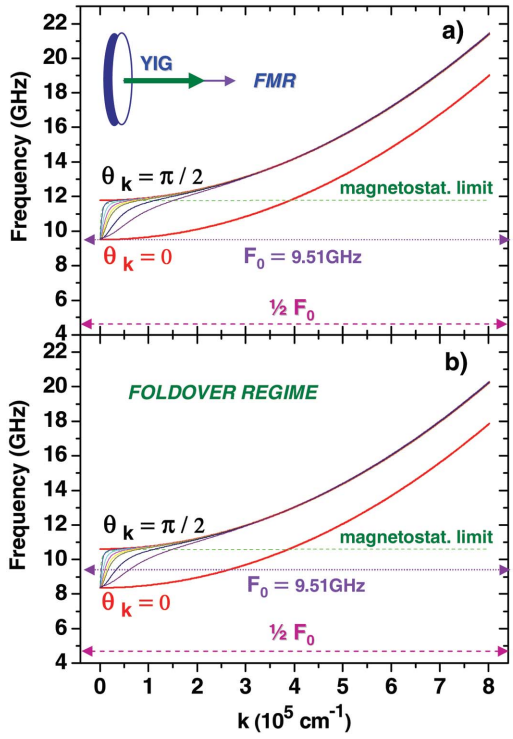

Figure 16
Magnetostatic and exchange spin wave dispersion spectrum: (*a*) at low pumping power; (*b*) in the foldover regime previously illustrated in Fig. 7.

interactions should strongly dominate over exchange interactions. This seems to be consistent with another argument: recall that the XDMR spectrum displayed in Fig. 12(*b*) was recorded at the *K*-edge of iron, and we shall see in the next section that the precessing magnetization component in the excited state can only be of orbital nature. Recall that spin–orbit interactions cannot be treated on the basis of the Heisenberg exchange Hamiltonian, whereas dipole–dipole interactions (that are responsible for magnetostatic waves) are quite commonly introduced to describe spin–orbit and orbit–orbit interactions.

4.2. Dynamics of orbital and spin components in excited states

We already pointed out earlier that the effective operator responsible for XMCD at a *K*-edge had a pure orbital nature. For electric dipole transitions, this immediately appears with a differential formulation of the XMCD sum-rules at *K*-edges (Strange, 1994; Ebert *et al.*, 1999),

$$[\Delta\sigma]_K = 3C_p \frac{\mathrm{d}}{\mathrm{d}\Delta E}\langle L_z\rangle_p = 3C_p\langle \ell_z\rangle_p, \tag{8}$$

in which $\Delta E = E_{\mathrm{RX}} - E_0$ is the energy of the photoelectron and C_p is a constant factor. The effective operators responsible for XMCD in electric quadrupole transitions were also derived by Carra and co-workers (Carra, König *et al.*, 1993): even in this case, one may show that the only terms which survive at a *K*-edge are still of orbital nature. The effective operator accounting for XMCD at the Fe *K*-edge in YIG could finally be decomposed as a sum of two terms (Goulon, Rogalev, Wilhelm *et al.*, 2005; Goulon *et al.*, 2006*a*), $\{\langle \ell_z\rangle_{4p} + \varepsilon\langle \ell_z\rangle_{3d}\}$.

At the spin–orbit split Y $L_{2,3}$-edges, one can similarly make use of differential operators (Strange, 1994; Ebert *et al.*, 1999)

$$\begin{aligned}[\Delta\sigma]_{L_3} &= \frac{C_d}{3N_{\mathrm{b}}}\frac{\mathrm{d}}{\mathrm{d}\Delta E}\left\{\langle L_z\rangle_d + \frac{2}{3}\langle S_z\rangle_d + \frac{7}{3}\langle T_z\rangle_d\right\}\\ &= \frac{C_d}{3N_{\mathrm{b}}}\left\{\langle \ell_z\rangle_d + \frac{2}{3}\langle s_z\rangle_d + \frac{7}{3}\langle t_z\rangle_d\right\}\end{aligned} \tag{9}$$

$$\begin{aligned}[\Delta\sigma]_{L_2} &= \frac{C_d}{6}\frac{\mathrm{d}}{\mathrm{d}\Delta E}\left\{\langle L_z\rangle_d - \frac{4}{3}\langle S_z\rangle_d - \frac{14}{3}\langle T_z\rangle_d\right\}\\ &= \frac{C_d}{6}\left\{\langle \ell_z\rangle_d - \frac{4}{3}\langle s_z\rangle_d - \frac{14}{3}\langle t_z\rangle_d\right\}\end{aligned} \tag{10}$$

in which $N_{\mathrm{b}} \simeq 2$ denotes the statistical branching ratio. Injecting (9) and (10) into the definition of ΔM_z, one would obtain an extended formulation of these sum-rules suitable for disentangling the precession dynamics of orbital and spin components (Goulon *et al.*, 2006*a*),

$$(1+3\eta)\tan^2\theta_0(L_3) = \tan^2\theta_{\mathrm{s}} + 3\eta\tan^2\theta_\ell, \tag{11}$$

$$(2-3\eta)\tan^2\theta_0(L_2) = 2\tan^2\theta_{\mathrm{s}} - 3\eta\tan^2\theta_\ell, \tag{12}$$

in which $\eta = \langle \ell_z\rangle_d/2\langle s_z\rangle_d$, and $\langle t_z\rangle_d/2\langle s_z\rangle_d$ was assumed here to be negligibly small. In (11) and (12), $\theta_0(L_3)$ and $\theta_0(L_2)$ are the effective precession angles measured at the Y L_3- and L_2-edges, whereas θ_{s} and θ_ℓ are the precession angles for the relevant spin and orbital magnetization components. This clearly shows that, at spin–orbit split *L*-edges, one cannot access the precession dynamics of the orbital components without resorting to additional approximations which are not needed at *K*-edges. As illustrated in Fig. 17, the XMCD studies carried out at the yttrium *L*-edges on pure or rare-earth-doped YIG films revealed that the induced spin magnetization of the Y *d*-DOS, *i.e.* $2\langle s_z\rangle_d$, largely exceeded the orbital contribution $\langle \ell_z\rangle_d$, so that $\eta \simeq -4.5 \times 10^{-3}$ at peak 1 and $\sim -6.8 \times 10^{-2}$ at peak 2.

On combining tentatively the XDMR and XMCD normalized cross sections according to equation (1), we obtained $\theta_0(L_3) \simeq 5.7^\circ$ for peak 1 at E_1 and $\sim 5.6^\circ$ for peak 2 at E_2. Given that the values which we obtained for η are quite small, one may guess that the precession angles $\theta_0(L_3)$ deduced from our XDMR measurements may directly yield a first estimation of the precession angle of the spin components of the magnetized *d*-projected DOS at the yttrium sites. This is also consistent with the additional results obtained at the Y L_2-edge since $\theta_0(L_2) \simeq 5.7^\circ$ for peak 1 at E_1.

Interestingly, it seems that the opening angles measured at the Fe *K*-edge and Y *L*-edges in YIG are of the same order of magnitude. Let us keep in mind that XDMR measurements at the Fe *K*-edge describe the precession of magnetized orbital components of *p*-projected DOS; similarly, XDMR measurements at the Y *L*-edges will describe the precession of spin polarized components of Y *d*-DOS but we expect the latter (induced) components to be rigidly coupled to the spin

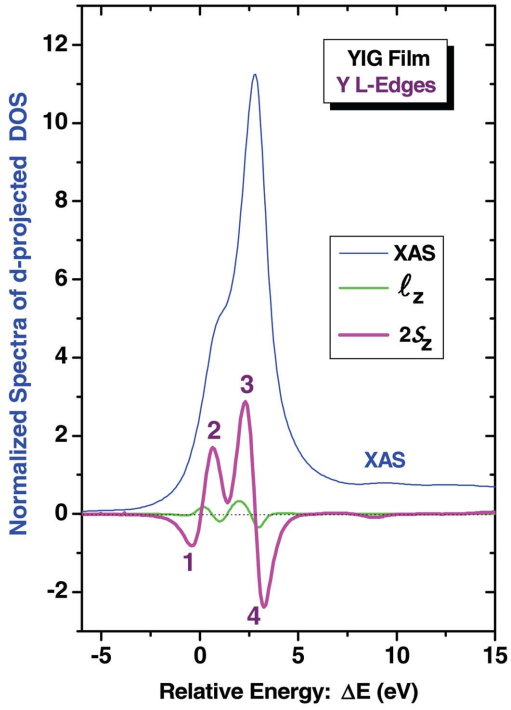

Figure 17
Orbital and spin magnetization components of yttrium *d*-DOS in the YIG thin film. All spectra displayed here were calculated using the differential XMCD sum-rules after careful corrections accounting for fluorescence reabsorption and polarization rates. Note the giant intensity of the white line in the XAS spectrum while the orbital magnetization component is very weak.

magnetization at the iron sites. Therefore, one may presume (Goulon *et al.*, 2007) that the precession of the spin and orbital magnetization components at the iron sites could be more or less rigidly coupled as well, *e.g.* like in acoustic modes of ferrimagnetic resonance. Many more systematic test experiments would obviously be required to validate this presumption and check whether our present finding is general or purely coincidental.

Finally, let us emphasize that we have no indication yet as to whether the spin and orbital magnetization components could precess with the same phase: only XDMR experiments in the transverse geometry could help us in clarifying this point which is essential in figuring out to what extent the spin and orbital magnetization components could remain almost aligned during precession as in the acoustic mode of ferrimagnetic resonance.

4.3. Future prospects

In our opinion, XDMR should not be seen as just another exotic inefficient way of detecting FMR. We expect XDMR to develop as a unique tool to disentangle at various absorbing edges the precession dynamics of either spin or orbital magnetization components. Given the high sensitivity of the heterodyne detection mode, one may even envisage determining the ellipticity of the precession trajectories of those magnetization components at various absorbing sites (Goulon *et al.*, 2006*a*). There is no doubt that the results reported in this paper will stimulate further investigations of forced precession at large opening angle. One option would be to exploit ultrashort high-power microwave pulses to study XDMR in a highly non-linear regime. Another option would be to explore with XDMR what happens in the SWASER regime of spin valves in which, according to Slonczewki and Berger (Slonczewski, 1996; Berger, 1996), electric currents flowing perpendicular to the magnetic layers could result in the creation of a negative Landau–Lifshitz-like relaxation torque.

On the other hand, extending XDMR measurements into the millimeter/submillimeter wave range would certainly revivify the interest of chemists for Van Vleck paramagnets on which still little is known. One may dream of detecting as well XDMR in ferrimagnetic and antiferromagnetic systems: measurements in the sub-THz range could perhaps permit establishing the questionable existence of new types of optic modes involving strongly coupled magnetization components of spin and orbital nature. Recall that, for antiferromagnetic systems, no static XMCD signal can be measured whereas antiferromagnetic resonance could possibly be measured using X-rays.

We are grateful to J. Ben Youssef and M. V. Indenbom (Laboratoire de Magnétisme de Bretagne) for providing us with pure and rare-earth-substituted YIG films prepared in Brest. Microfluorescence analyses were performed at the ESRF by I. Snigireva. Invaluable technical assistance by M.-C. Dominguez, S. Feite and P. Voisin during the whole project is warmly acknowledged here. We also benefited occasionally from the help of Ch. Hervé (ESRF/Digital Electronics group) and J. Marcus (Institut Néel, Grenoble). Finally, we greatly appreciated the constant support and encouragements of Y. Petroff and F. Sette during the critical phase of the XDMR project.

References

Arena, D. A., Vescovo, E., Kao, C.-C., Guan, Y. & Bailey, W. A. (2006). *Phys. Rev. B*, **74**, 064409(1–7).
Bailey, W. E., Cheng, L., Keavney, D. J., Kao, C.-C., Vescovo, E. & Arena, D. A. (2004). *Phys. Rev. B*, **70**, 172403(1–4).
Berger, L. (1996). *Phys. Rev. B*, **54**, 9353–9358.
Berteaud, A.-J. & Pascard, H. (1966). *J. Appl. Phys.* **37**, 2035–2043.
Bertotti, G., Serpico, C. & Mayergoyz, I. D. (2001). *Phys. Rev. Lett.* **86**, 724–727.
Bloembergen, N. & Wang, S. (1954). *Phys. Rev.* **93**, 72–83.
Boero, G., Rusponi, S., Bencok, P., Popovic, R. S., Brune, H. & Gambardella, P. (2005). *Appl. Phys. Lett.* **87**, 152503(1–3).
Borovik-Romanov, A. S., Kreines, N. M., Laiho, R., Levola, T. & Zhotikov, V. G. (1980). *J. Phys. C*, **13**, 879–885.
Carra, P., König, H., Thole, B. T. & Altarelli, M. (1993). *Physica B*, **192**, 182–190.
Carra, P., Thole, B. T., Altarelli, M. & Wang, X. D. (1993). *Phys. Rev. Lett.* **70**, 694–697.
Charbois, V. (2003). PhD thesis. Université Paris-VII Denis Diderot, France.
Damon, R. W. (1953). *Rev. Mod. Phys.* **25**, 239–244.
Ebert, H., Popescu, V. & Ahlers, D. (1999). *Phys. Rev. B*, **60**, 7156–7165.

Fletcher, R. C., LeCraw, R. C. & Spencer, E. G. (1960). *Phys. Rev.* **117**, 955–963.
Froncisz, W. & Hyde, J. S. (1982). *J. Magn. Reson.* **47**, 515–521.
Gilleo, M. A. (1980). *Ferromagnetic Materials*, Vol. 2, edited by E. P. Wohlfarth, ch. 1, pp. 1–53. Amsterdam: North Holland.
Gnatzig, K., Dötsch, H., Ye, M. & Brockmayer, A. (1987). *J. Appl. Phys.* **62**, 4839–4843.
Goulon, J., Rogalev, A., Gauthier, Ch., Goulon-Ginet, C., Pasté, S., Signorato, R., Neumann, C., Varga, L. & Malgrange, C. (1998). *J. Synchrotron Rad.* **5**, 232–238.
Goulon, J., Rogalev, A., Goujon, G., Gauthier, Ch., Moguiline, E., Solé, A., Feite, S., Wilhelm, F., Jaouen, N., Goulon-Ginet, Ch., Dressler, P., Rohr, P., Lampert, M.-O. & Henck, R. (2005). *J. Synchrotron Rad.* **12**, 57–69.
Goulon, J., Rogalev, A., Wilhelm, F., Brouder, Ch., Yaresko, A., Ben Youssef, J. & Indenbom, M. V. (2007). *J. Magn. Magn. Mater.* Submitted.
Goulon, J., Rogalev, A., Wilhelm, F., Jaouen, N., Goulon-Ginet, C. & Brouder, Ch. (2006*a*). *Eur. Phys. J. B*, **53**, 169–184.
Goulon, J., Rogalev, A., Wilhelm, F., Jaouen, N., Goulon-Ginet, C., Goujon, G., Ben Youssef, J. & Indenbom, M. V. (2005). *JETP Lett.* **82**, 791–796.
Goulon, J., Rogalev, A., Wilhelm, F., Jaouen, N., Goulon-Ginet, C., Goujon, G., Ben Youssef, J. & Indenbom, M. V. (2006*b*). *J. Electron Spectrosc. Relat. Phenom.* [doi:10.1016/j.elspec.2006.11.047].
Gratton, E. (1992). *AIP Conf. Proc.* **258**, 453–464.
Guan, Y., Bailey, W. A, Kao, C.-C., Vescovo, E. & Arena, D. A. (2006). *J. Appl. Phys.* **99**, 08J305(1–3).
Gurevich, A. G. & Melkov, G. A. (1996). *Magnetization Oscillations and Waves.* Boca Raton: CRC Press.
Hanlon, J. T. & Dillon, J. F. (1965). *J. Appl. Phys.* **36**, 1269–70.
Hartmann-Boutron, F. (1964). *J. Appl. Phys. Suppl.* **35**, 889–891.
Kasuya, T. & LeCraw, R. C. (1961). *Phys. Rev. Lett.* **5**, 223–225.
Lenz, K., Wende, H., Kuch, W., Baberschke, K., Nagy, K. & Jánossy, A. (2006). *Phys. Rev. B*, **73**, 144424.
Loubens, G. de, Naletov, V. V. & Klein, O. (2005). *Phys. Rev. B*, **71**, 180411R.
Pfenninger, S., Forrer, J. & Schweiger, A. (1988). *Rev. Sci. Instrum.* **59**, 752–760.
Puzic, A., Van Waeyenberge, B., Kang Wei, C., Fischer, P., Stoll, H., Schütz, G., Tiliszcak, T., Rott, K., Brückl, H., Reiss, G., Neudecker, I., Haug, T., Buess, M. & Back, Ch. H. (2005). *J. Appl. Phys.* **97** 10E704.
Rogalev, A., Goulon, J., Benayoun, G., Elleaume, P., Chavanne, J., Penel, Ch. & van Vaerenbergh, P. (1999). *Proc. SPIE*, **3773**, 275–283.
Rogalev, A., Wilhelm, F., Jaouen, N., Goulon, J. & Kappler, J. P. (2006). *Magnetism: a Synchrotron Radiation Approach, Lecture Notes in Physics*, Vol. 697, edited by E. Beaurepaire, H. Bulou, F. Scheurer and J. P. Kappler, pp. 71–94. Berlin: Springer Verlag.
Schütz, G., Wagner, W., Kienle, P., Zeller, R., Frahm, R. & Materlick, G. (1987). *Phys. Rev. Lett.* **58**, 737–740.
Slonczewski, J. C. (1996). *J. Magn. Magn. Mater.* **159**, L1–L7.
Sparks, M. (1964). *Ferromagnetic Relaxation Theory.* New York: McGraw-Hill.
Strange, P. (1994). *J. Phys. Condens. Matter*, **6**, L491–L495.
Suhl, H. (1957). *J. Phys. Chem. Solids*, **1**, 209–227.
Suhl, H. (1959). *J. Appl. Phys.* **30**, 1961–1964.
Thole, B. T., Carra, P., Sette, S. & Van der Laan, G. (1992). *Phys. Rev. Lett.* **68**, 1943–1946.
Van Vleck, J. H. (1964). *J. Appl. Phys. Suppl.* **35**, 882–888.
Vittoria, C., Lubitz, P., Hansen, P. & Tolksdorf, W. (1985). *J. Appl. Phys.* **57**, 3699–3700.
Yong An, S., Krivosik, P., Kraemer, M. A., Olson, H. M., Nazarov, A. V. & Patton, C. E. (2004). *J. Appl. Phys.* **96**, 1572–1580.